AMERICAN ACADEMY OF OPHTHALMOLOGY®

Assessing Surface Shapes of the Optic Nerve Head and Peripapillary Retinal Nerve Fiber Layer in Glaucoma with Artificial Intelligence

Chhavi Saini, MD,[1] Lucy Q. Shen, MD,[1] Louis R. Pasquale, MD,[2] Michael V. Boland, MD, PhD,[1] David S. Friedman, MD, PhD,[1] Nazlee Zebardast, MD, MSc,[1] Mojtaba Fazli, PhD,[3] Yangjiani Li, MD,[3,4] Mohammad Eslami, PhD,[3] Tobias Elze, PhD,[3] Mengyu Wang, PhD[3]

Purpose: To assess 3-dimensional surface shape patterns of the optic nerve head (ONH) and peripapillary retinal nerve fiber layer (RNFL) in glaucoma with unsupervised artificial intelligence (AI).

Design: Retrospective study.

Participants: Patients with OCT scans obtained between 2016 and 2020 from Massachusetts Eye and Ear.

Methods: The first reliable Cirrus (Carl Zeiss Meditec, Inc) ONH OCT scans from each eye were selected. The ONH and RNFL surface shape was represented by the vertical positions of the inner limiting membrane (ILM) relative to the lowest ILM vertical position in each eye. Nonnegative matrix factorization was applied to determine the ONH and RNFL surface shape patterns, which then were correlated with OCT and visual field (VF) loss parameters and subsequent VF loss rate. We tested whether using ONH and RNFL surface shape patterns improved the prediction accuracy for associated VF loss and subsequent VF loss rates measured by adjusted r^2 and Bayesian information criterion (BIC) difference compared with using established OCT parameters alone.

Main Outcome Measures: Optic nerve head and RNFL surface shape patterns and prediction of the associated VF loss and subsequent VF loss rates.

Results: We determined 14 ONH and RNFL surface shape patterns using 9854 OCT scans from 5912 participants. Worse mean deviation (MD) was most correlated ($r = 0.29$ and $r = 0.24$, Pearson correlation; each $P < 0.001$) with lower coefficients of patterns 10 and 12 representing inferior and superior para-ONH nerve thinning, respectively. Worse MD was associated most with higher coefficients of patterns 5, 4, and 9 ($r = -0.16$, $r = -0.13$, and $r = -0.13$, respectively), representing higher peripheral ONH and RNFL surfaces. In addition to established ONH summary parameters and 12−clock-hour RNFL thickness, using ONH and RNFL surface patterns improved (BIC decrease: 182, 144, and 101, respectively; BIC decrease ≥ 6; strong model improvement) the prediction of accompanied MD (r^2 from 0.32 to 0.37), superior (r^2 from 0.27 to 0.31), and inferior (r^2 from 0.17 to 0.21) paracentral loss and improved (BIC decrease: 8 and 8, respectively) the prediction of subsequent VF MD loss rates (r^2 from 0 to 0.13) and inferior paracentral loss rates (r^2 from 0 to 0.16).

Conclusions: The ONH and RNFL surface shape patterns quantified by unsupervised AI techniques improved the structure−function relationship and subsequent VF loss rate prediction. *Ophthalmology Science 2022;2:100161 © 2022 by the American Academy of Ophthalmology. This is an open access article under the CC BY-NC-ND license (http://creativecommons.org/licenses/by-nc-nd/4.0/).*

Supplemental material available at www.ophthalmologyscience.org.

Identification of glaucomatous structural damage traditionally has relied on optic nerve head (ONH) parameters, including cup-to-disc ratio (CDR), disc tilt, disc ovality, and disc torsion assessed based on 2-dimensional (2-D) fundus imaging.[1,2] Two-dimensional images of the ONH are not optimal to capture the subsurface structural changes, and studies have shown that estimates of clinically perceived anatomic structures including the disc margin based on stereophotographs are inaccurate.[3] Subsequently, imaging technologies like confocal scanning laser ophthalmoscopy have provided quantitative stereometric parameters and information on ONH and peripapillary retinal contour.[4] With the advent of OCT imaging techniques, we now have considerable insight into 3-dimensional (3-D) ONH anatomic features, such as the position and shape of the lamina cribrosa and neuroretinal rim parameters, which have been quantified and associated with glaucoma.[5−10] Most recently, Panda et al[11] developed a deep learning model to segment 3 neural-tissue and 4 connective-tissue layers of the ONH. The segmented images were then processed by a customized autoencoder network (a neural network that can be used to learn low-dimensional features from high-dimensional data) for feature reduction. Structure phenotype as determined by unsupervised machine learning based

https://doi.org/10.1016/j.xops.2022.100161
ISSN 2666-9145/22

on the reduced features from the deep autoencoder was associated with glaucoma diagnosis.[11] Although this work on the 3-D structural phenotype of the ONH is promising, it involved a time-consuming step of manual delineation of the 3-D ONH structure, which impedes its applicability. In addition, the mapping between structural phenotypes determined from structural features extracted by autoencoder, principal component analysis, and uniform manifold approximation and projection and the individual 3-D ONH structures remains limited for clinical interpretation.

In this study, we aimed to quantify the ONH and retinal nerve fiber layer (RNFL) surface structure represented by the inner limiting membrane (ILM) using an unsupervised artificial intelligence (AI) method termed nonnegative matrix factorization (NMF). The ILM boundary is provided by the OCT manufacturer's segmentation software. We specifically chose NMF to quantify the ONH and RNFL surface shape because it is well suited to determine representative linear patterns with sparse features for nonnegative measurements,[12,13] which are expected to be more clinically interpretable than nonlinear patterns determined from reduced features extracted by deep autoencoders. The ONH and RNFL surface shape patterns determined by NMF were associated with structural, functional, and other established glaucoma diagnostic parameters. We also determined whether using the ONH and RNFL surface shape patterns improved the prediction of visual field (VF) loss and subsequent VF loss rate compared with established OCT parameters alone.

Methods

The study was approved by the Massachusetts Eye and Ear Institutional Review Board and adhered to the tenets of the Declaration of Helsinki. Given the retrospective nature of the study, the need for informed consent was waived.

Study Design and Data

OCT scans of the ONH from a spectral-domain (SD) OCT device (Cirrus; Carl Zeiss Meditec, Inc) with signal strength of ≥ 6 were used.[14,15] The earliest available OCT scan from each eye was analyzed. All OCT scans were represented in right-eye format for analysis. The 6 $\times$ 6-mm ONH cube scan comprising 200 B-scans with 200 A-scans per B-scan was used to construct the 2-D ILM topographical maps, and any scans with ONH centers deviating > 0.3 mm from the scan center were excluded to ensure data availability across all scans. The ONH and RNFL surface shape was represented as the relative vertical position of the ILM with respect to the lowest vertical ILM position in each eye (Fig 1A). Anatomically, higher position of the ONH and RNFL surface represents more anterior structures and vice versa (Fig 1B, C). Additionally, at the rim of the ONH, ILM is continuous with the prelaminar tissue inside the ONH and continues as the ILM of Elschnig[16,17]; however, for the purpose of this study, we refer to the term *ILM*, based on the positions of either ILM (outside the ONH) or its continuation (inside the ONH).

Electronic medical records were used to obtain demographic and ophthalmic characteristics for all study participants. For the cross-sectional analyses, glaucoma diagnosis codes recorded before or no later than 6 months from the OCT test date were selected. Specifically, diagnosis codes for suspect glaucoma, primary open-angle glaucoma, primary angle-closure glaucoma, and secondary or unspecified glaucoma subtypes were used to identify the glaucoma subtypes. Spherical equivalent measured within 3 months and intraocular pressure (IOP) information from the day of the OCT test date were used. If multiple clinical measurements satisfied our inclusion criteria, the measurement closest to the OCT imaging was selected. Reliable (fixation losses, $\leq 33\%$; false-positive and false-negative rates, $\leq 20\%$)[18–20] Swedish Interactive Threshold Algorithm standard 24-2 VFs (Humphrey Field Analyzer; Carl Zeiss Meditec, Inc) acquired within 3 months from the OCT test date were included for structure–function correlation modeling. Specifically, mean deviation (MD) and superior and inferior paracentral loss were used to measure accompanied VF loss. Superior paracentral loss total deviation (TD) was defined by the average TD at the central upper 2 locations closest to fixation, and inferior paracentral loss was defined by the average TD at the central lower 2 locations closest to fixation.

For the longitudinal analyses, reliable (fixation losses, $\leq 33\%$; false-positive and false-negative rates, $\leq 20\%$)[18–20] VF results acquired at least 3 months after the OCT test date were selected. Only eyes with at least 5 VF results were used for longitudinal analyses. The VF loss rate was calculated by regressing the metrics of MD and superior and inferior paracentral loss over time.

Primary Outcome Measures

The primary outcome measures were (1) the ONH and RNFL surface shape patterns quantified by unsupervised AI, (2) the correlation relationships between the ONH and RNFL surface shape patterns and established glaucoma diagnostic parameters, and (3) the regression models using the ONH and RNFL surface shape patterns to predict accompanied VF loss and subsequent VF loss rate.

Statistical Analysis

All statistical analyses were conducted using R software, version 3.4.3 (R Foundation for Statistical Computing). Nonnegative matrix factorization, an unsupervised AI method, was applied to assess the ONH and RNFL surface shape patterns.[12,13,21] Pearson correlations adjusted for the intereye correlation with linear mixed models were calculated between ONH and RNFL surface shape patterns and established glaucoma diagnostic parameters, including the glaucoma subtype, IOP, spherical equivalent, VF MD, and structural parameters provided by the OCT software, including average RNFL thickness (RNFLT), average CDR, vertical CDR, cup volume, disc area, and rim area. Using linear mixed models to account for the intereye correlation, the ONH and RNFL surface shape patterns were used to predict the accompanied VF loss cross-sectionally and subsequent VF loss rates longitudinally measured by the MD slope, TD slope at the central upper 2 locations, and TD slope at the central lower 2 locations. Redundant features were removed by model selection with stepwise regression using the Bayesian information criterion (BIC). We compared whether the addition of ONH and RNFL surface shape patterns to the model with established OCT parameters improved the prediction of accompanied VF loss. Adjusted r^2 values penalizing for the number of predictors after model selection were used to measure prediction performance of the regression models. The BIC difference was used to compare quantitatively the prediction performance between different regression models by separately using and combining 3 sets of features, including ONH and RNFL surface shape patterns, ONH summary parameters, and RNFLT parameters. Note that a BIC decrease of ≥ 6 is considered a strong model improvement. *P* value correction for multiple comparisons by the false discovery rate method was applied for all analyses with

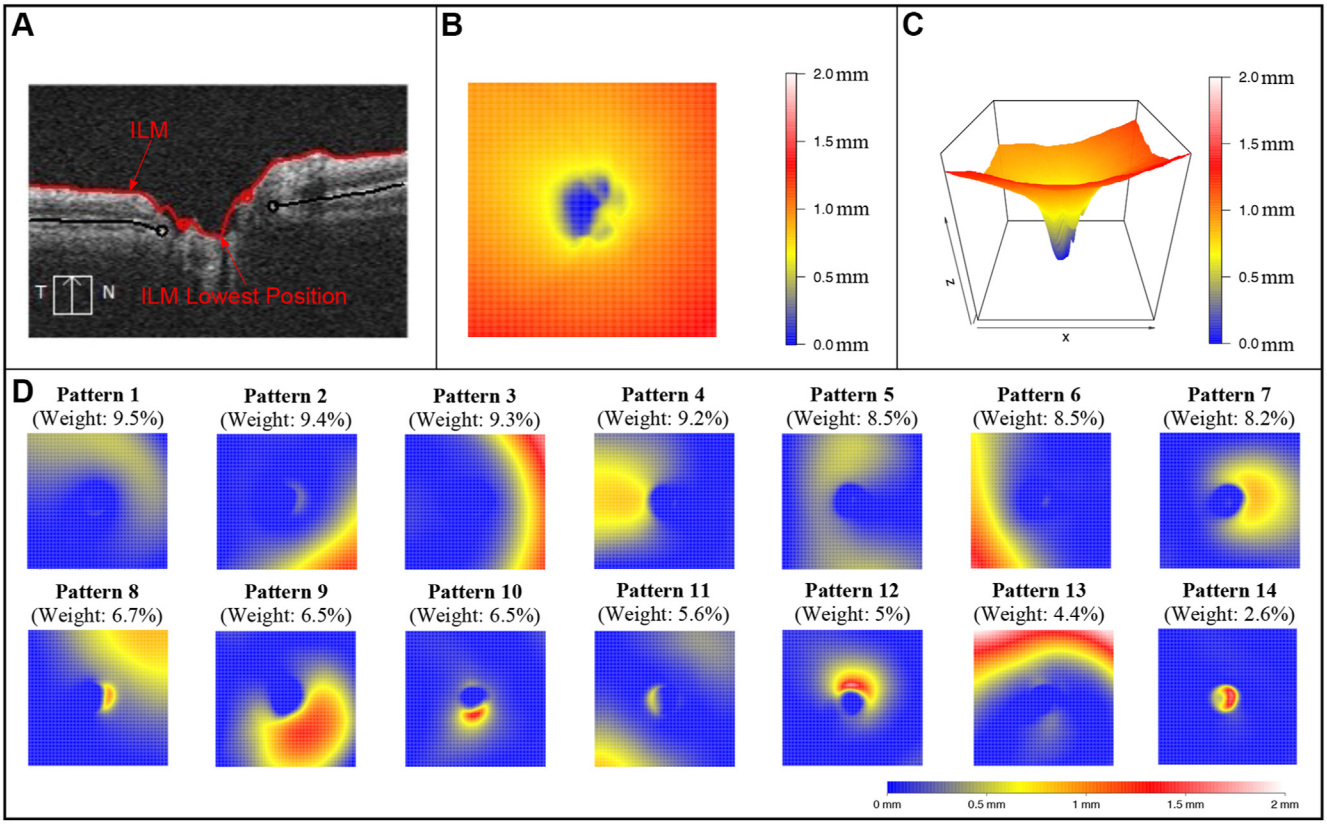

Figure 1. **A**, OCT scan showing the vertical positions of the inner limiting membrane (ILM) with respect to the lowest continuation of the vertical ILM position optic nerve head (ONH). **B**, **C**, Example of the ONH and RNFL surface shape structure in (**B**) 2-dimensional and (**C**) 3-dimensional heatmaps. **D**, Fourteen ONH and RNFL surface shape patterns identified with an unsupervised artificial intelligence method, nonnegative matrix factorization.

multiple comparisons, and a false discovery rate-corrected *P* value of < 0.05 was considered significant and is reported throughout.[22] Of note, given that BIC model selection is more stringent, we also performed our analysis for VF loss rate prediction using the Akaike information criterion because of our relatively small sample size for this longitudinal analysis.

Results

Patient Characteristics

To determine the ONH and RNFL surface shape patterns, 9854 OCT scans from 9854 eyes of 5912 participants were used. The mean ± standard deviation age of the participants at the time of OCT imaging was 63.7 ± 15.3 years, and 56.3% were women. Of the 5912 participants, 63.5% self-identified as White (Table 1). Among the 5294 participants with glaucoma diagnosis information, 50.4% had a diagnosis of suspect glaucoma, 30.0% had a diagnosis of primary open-angle glaucoma, 3.5% had a diagnosis of primary angle-closure glaucoma, 9.2% had a diagnosis of other types of open-angle glaucoma, and 6.9% had a diagnosis of secondary or unspecified glaucoma subtypes. Intraocular pressure measurements from the same day as the OCT imaging date were available for 8563 eyes of 5177 participants with an average IOP of 15.5 ± 4.4 mmHg. Of the 9854 eyes, the global average RNFLT and vertical CDR measured by OCT were 78.8 ± 16.2 μm and 0.63 ± 0.17, respectively. Visual field findings acquired within 3 months from the OCT imaging date were available for 3295 eyes of 2290 participants, and the MD, average TD at the central upper 2 locations, and average TD at the central lower 2 locations were −4.9 ± 6.9 decibels (dB), −4.4 ± 8.0 dB, and −3.4 ± 6.4 dB, respectively. Spherical equivalent measurements obtained within 3 months from the OCT imaging date were available for 2330 eyes of 1489 participants, with average spherical equivalent of −0.8 ± 3.5 diopters.

The ONH and RNFL Surface Shape Patterns

Applying the NMF method, we identified 14 ONH and RNFL surface shape patterns (Fig 1D) from the 3-D ONH and RNFL surface shape structure (Fig 1B, C) in each eye. The ONH and RNFL surface shape patterns were represented in the right-eye format and were ordered by their respective average decomposition weights over all 9854 OCT scans from 9854 eyes. The yellow and red regions of the ONH and RNFL surface patterns indicate higher positions and where large variations exist among different eyes. Therefore, these regions were considered to be relatively informative regarding the ONH and RNFL surface shape structure. By contrast, blue denoted lower ILM positions and where minimal variations existed among

Table 1. Demographics and Baseline Characteristics of the Patients Included in the Study

Characteristic	Data
No. of patients (eyes)	5912 (9854)
Age (yrs)	63.7 ± 15.3
Female sex	56.3
Race	
Black	12.5
American Indian or Alaska native	0.1
Asian	7.1
European	63.5
Native Hawaiian or other Pacific Islander	0.1
Mixed or other race	6.3
Unknown or not reported	10.4
Glaucoma diagnosis*	
Suspect glaucoma	50.4
Primary open-angle glaucoma	30.0
Primary angle-closure glaucoma	3.5
Other open-angle glaucoma	9.2
Secondary or unspecified glaucoma subtype	6.9
Intraocular pressure (mmHg)†	15.5 ± 4.4
OCT parameters	
Average RNFL thickness (μm)	78.8 ± 16.2
Rim area (mm^2)	1.0 ± 0.3
Disc area (mm^2)	1.9 ± 0.4
Average cup-to-disc ratio	0.64 ± 0.16
Vertical cup-to-disc ratio	0.63 ± 0.17
Cup volume (mm^3)	0.33 ± 0.27
VF parameters (dB)‡	
Average HVF MD	−4.9 ± 6.9
Average TD at central upper 2 VF locations	−4.4 ± 8.0
Average TD at central lower 2 VF locations	−3.4 ± 6.4
Spherical equivalent (diopters)§	−0.8 ± 3.5

dB = decibel; HVF = Humphrey Visual Field; MD = mean deviation; RNFL = retinal nerve fiber layer; TD = total deviation; VF = visual field. Data are presented as mean ± standard deviation or percentage, unless otherwise indicated.
*Available for 89.5% of patients, recorded before or no later than 6 months after the OCT imaging date.
†Available for 87.6% of patients, measured on the same day as the OCT imaging date.
‡Available for 38.7% of patients, with VFs acquired within 3 months from the OCT imaging date.
§Available for 25.2% patients, recorded within 3 months from the OCT imaging date.

different eyes and was considered to be the relatively uninformative region in the ONH and RNFL surface shape structure. It is important to note that each ONH and RNFL surface shape structure could be decomposed into these 14 patterns, and a higher coefficient or weight of a specific ONH and RNFL surface shape pattern indicates the higher ILM position in the relatively informative regions of that pattern and vice versa. More specifically, patterns 1 and 13 represent the ILM position variation in the superior peripheral region around the ONH; patterns 3 and 6 represent the ILM position variation in the nasal and temporal peripheral region around the ONH; patterns 2, 8, and 11 represent the ILM position variation in the inferior-nasal, superior-nasal, and inferior-temporal peripheral regions around the ONH; patterns 4 and 7 represent the ILM position variation in temporal and nasal inner regions around the ONH; pattern 9 represents the ILM variation in the inferior-nasal inner region around the ONH; patterns 10 and 12 represent the ILM position variation in the inferior and superior para-ONH region; pattern 5 represents the ILM position variation in the arcuate region across the superior, temporal, and inferior regions around the ONH; and pattern 14 represents the ILM position variation within the ONH. Figure 2A–F illustrates an example of ONH and RNFL surface shape structure with a low coefficient (0) of pattern 10 (representing inferior para-ONH nerve thinning) plotted in 2-D and 3-D (Fig 2D, E, respectively). This eye exhibited conspicuous RNFL loss in clock hours 6 and 7 and corresponding superior VF defect (Fig 2C, F, respectively). Figure 2G–L illustrates another example of ONH and RNFL surface shape structure with a low coefficient (0) of pattern 10 (representing inferior para-ONH nerve thinning) in a myopic patient (spherical equivalent, −7 diopter) plotted in 2-D and 3-D (Fig 2J, K, respectively). Again, this eye showed substantial RNFL loss in clock hours 6 and 7 and severe superior VF loss. Additionally, this patient also demonstrated a low coefficient (0.1) of pattern 6, corresponding to lower ILM position variation in the temporal peripheral region and ONH tilt in the nasal direction, evidenced by the comparison of the 3-D images between Figure 2K (myopic example) and Figure 2E (nonmyopic example).

Correlation with Established Glaucoma Diagnostic Parameters and OCT Parameters

To better understand the pathophysiologic implications of the ONH and RNFL surface shape patterns, we correlated the ONH and RNFL surface shape patterns with various established glaucoma diagnostic parameters and OCT parameters (Fig 3). Worse VF MD was associated most ($P < 0.001$ for all) with lower coefficients of patterns 10 ($r = 0.29$) and 12 ($r = 0.24$) representing the inferior and superior para-ONH nerve thinning, respectively. Lower coefficients of pattern 10 depict a lower position of the ILM in the red region of this pattern, which represents RNFL loss near the inferior ONH region. Complementary to this, worse VF MD also was associated with lower coefficients of pattern 12 ($r = 0.24$), representing RNFL loss in the superior sector. Interestingly, VF MD was inversely associated with patterns 5 ($r = -0.16$), 4 ($r = -0.13$), 9 ($r = -0.13$), 2 ($r = -0.12$), and 6 ($r = -0.12$), representing higher ILM in the arcuate region across superior, temporal, and inferior areas; temporal inner region; inferior-nasal inner region; inferior-nasal peripheral region; and temporal peripheral region around the ONH, respectively. Thinner average global RNFL was associated most ($P < 0.001$ for all) with lower coefficients of patterns 10 ($r = 0.28$) and 12 ($r = 0.21$), representing the inferior and superior para-ONH nerve thinning, respectively, and with higher coefficients of patterns 4 ($r = -0.22$) and 11 ($r = -0.18$), representing higher ILM in the temporal inner region and inferior-temporal peripheral regions around the ONH, respectively. The greater average CDR was associated most ($P < 0.001$ for all) with lower coefficients of patterns 14 ($r = -0.59$) and 12 ($r = -0.26$), representing deep cups and superior

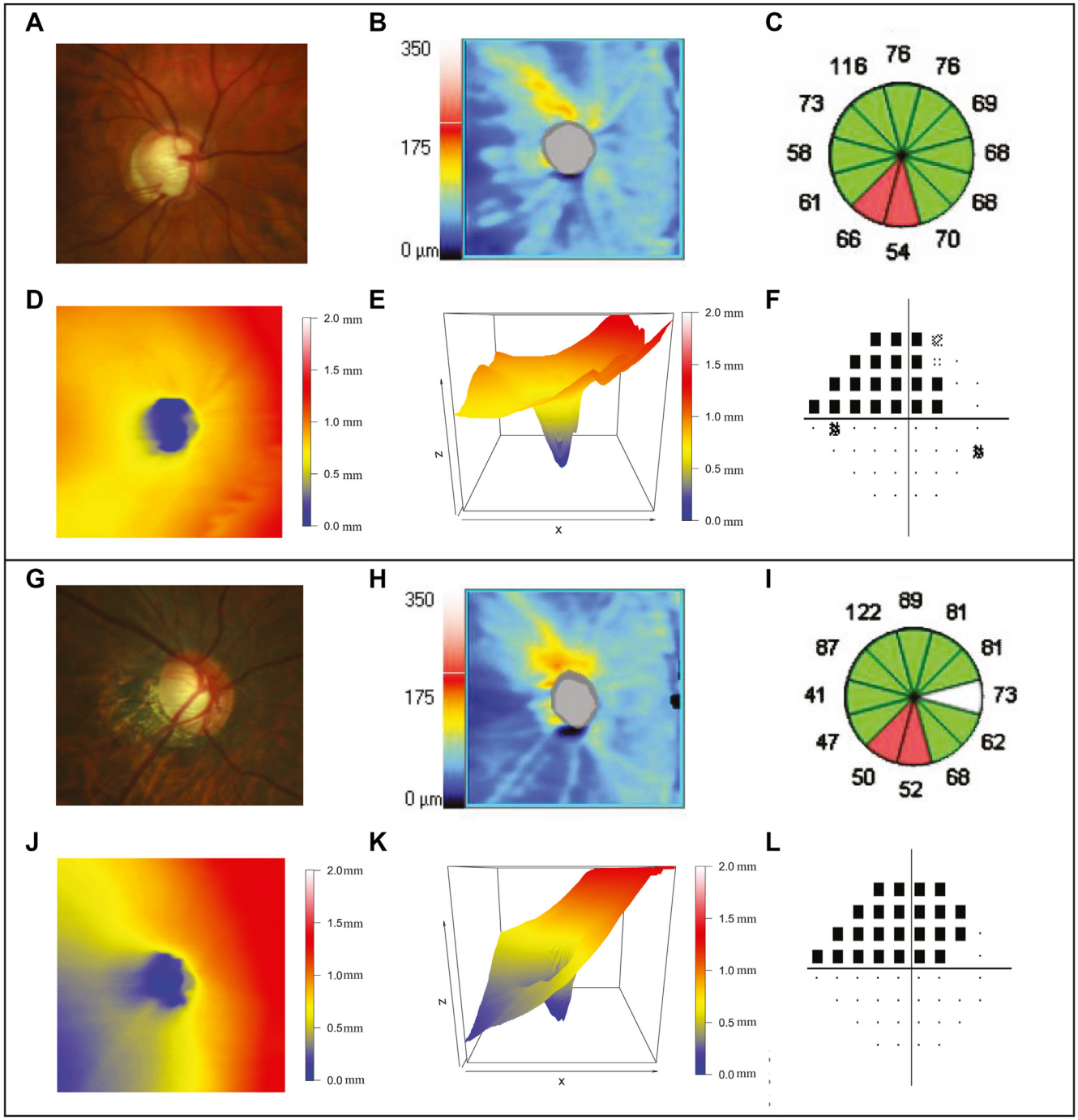

Figure 2. **A**–**E**, Examples of (**A**) a fundus photograph, (**B**) a retinal nerve fiber layer (RNFL) thickness map, (**C**) RNFL clock hours, and optic nerve head (ONH) and RNFL surface shape structure in a patient with a low coefficient (0) of pattern 10 plotted in (**D**) 2-dimensional (2-D) and (**E**) 3-dimensional (3-D) graphs. **F**, Corresponding pattern deviation plot from the 24-2 Humphrey visual field of this patient. **G**–**K**, Examples of (**G**) a fundus photograph, (**H**) an RNFL thickness map, (**I**) RNFL clock hours, and ONH and RNFL surface shape structure in a patient with myopia and a low coefficient (0) of pattern 10 plotted in (**J**) 2-D and (**K**) 3-D maps. **L**, Corresponding pattern deviation plot from the 24-2 Humphrey visual field of this patient. This patient also showed a low coefficient (0.1) of pattern 6, which corresponds to the ONH tilted up toward the nasal direction.

para-ONH nerve thinning, respectively, and with higher coefficients of patterns 5 ($r = 0.58$), 7 ($r = 0.54$), and 4 ($r = 0.52$), representing higher ILM in the arcuate region across superior, temporal and inferior areas; higher ILM in the nasal inner region; and higher ILM in the temporal inner region around ONH region, respectively. Myopia (lower spherical equivalent) was associated most ($P < 0.001$ for all) with lower coefficients of pattern 6 ($r = 0.11$),

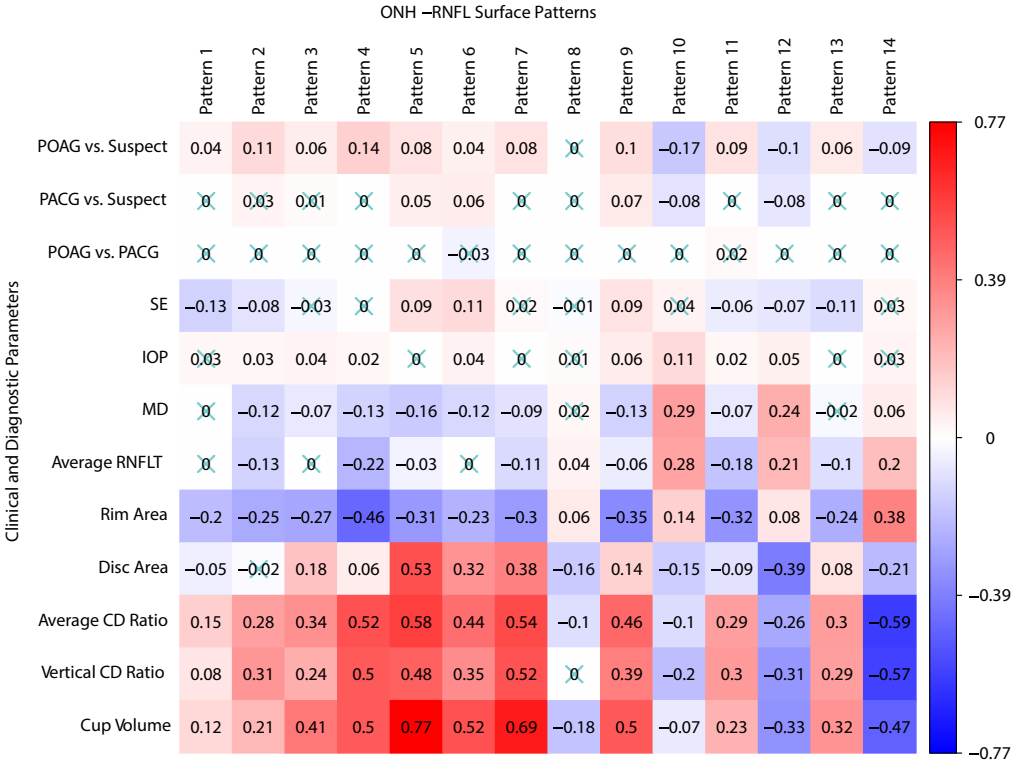

Figure 3. Correlations of the optic nerve head (ONH) and retinal nerve fiber layer surface shape patterns with various established glaucoma diagnostic parameters and OCT parameters, including visual field mean deviation (MD), glaucoma diagnosis, intraocular pressure (IOP), spherical equivalent (SE), and ONH summary parameters from the OCT analysis report. Numbers in the boxes denote the correlation coefficients, and insignificant correlations have been crossed out. CD = cup-to-disc; PACG = primary angle-closure glaucoma; POAG = primary open-angle glaucoma; RNFLT = retinal nerve fiber layer thickness.

representing lower ILM in the temporal peripheral region and with higher coefficients of pattern 1 ($r = -0.13$), representing higher ILM in the superior peripheral region, which may be explained by disc tilt (Fig 2G–L).

Interestingly, lower coefficients of pattern 10 (Supplemental Fig 1) were associated most ($P < 0.001$ for all) with clock hour 7 ($r = 0.42$) and 6 ($r = 0.29$) RNFLT, which are the clock-hour sectors closest to the inferior thinning location in the para-ONH region. Similarly, lower coefficients of pattern 12 were associated most ($P < 0.001$ for all) with the clock hour 10 ($r = 0.27$) and 11 ($r = 0.27$) RNFLT, which are the clock-hour sectors closest to the superior thinning location in the para-ONH region.

The ONH and RNFL Surface Shape Patterns and Prediction of Accompanying VF Parameters

Figure 4A shows the heatmap of adjusted r^2 values for different linear models that predicted the accompanied VF loss (including MD, average TD at the central upper 2 locations, and average TD at the central lower 2 locations) using the 3 groups of structural features, including ONH summary parameters, clock-hour RNFLTs, and ONH and RNFL surface shape patterns, separately or in combination. Using ONH and RNFL surface shape patterns in addition to the ONH summary parameter and 12 clock-hour RNFLTs improved the prediction of accompanied VF MD (r^2 from 0.32 to 0.37) and superior (r^2 from 0.27 to 0.31) and inferior (r^2 from 0.17 to 0.21) paracentral loss (Fig 4A). The prediction improvement was strong based on the model comparison using BIC (BIC decrease of 182, 144, and 101, respectively). Note that BIC decrease of ≥ 6 is considered a significant improvement.

Figure 4B–D shows the optimal ONH and RNFL surface shape patterns that best predict the VF loss parameters. Figure 4E–G shows the optimal structural features selected from the model combining 3 groups of structural features, including ONH summary parameters, clock-hour RNFLT, and ONH and RNFL surface shape patterns, that best predicted the VF loss. The numbers noted on top of the bars represent the respective statistical significance of each parameter, which were measured by the magnitude of BIC increase when that parameter was removed from the optimal model, and the direction of the bar represents the direction of the coefficient for that parameter when included in the optimal model. The greater BIC increase on removal of the variable from the model indicates more importance of that parameter for predicting the VF loss. A BIC increase of ≥ 6, when removing the parameter from the model, indicates that the parameter is associated strongly with the outcome. The top 4 most important parameters ($P < 0.001$ for all) for predicting various aspects of VF loss were (1) for worse MD (Fig 4B), lower pattern 10 (the inferior para-ONH nerve), lower

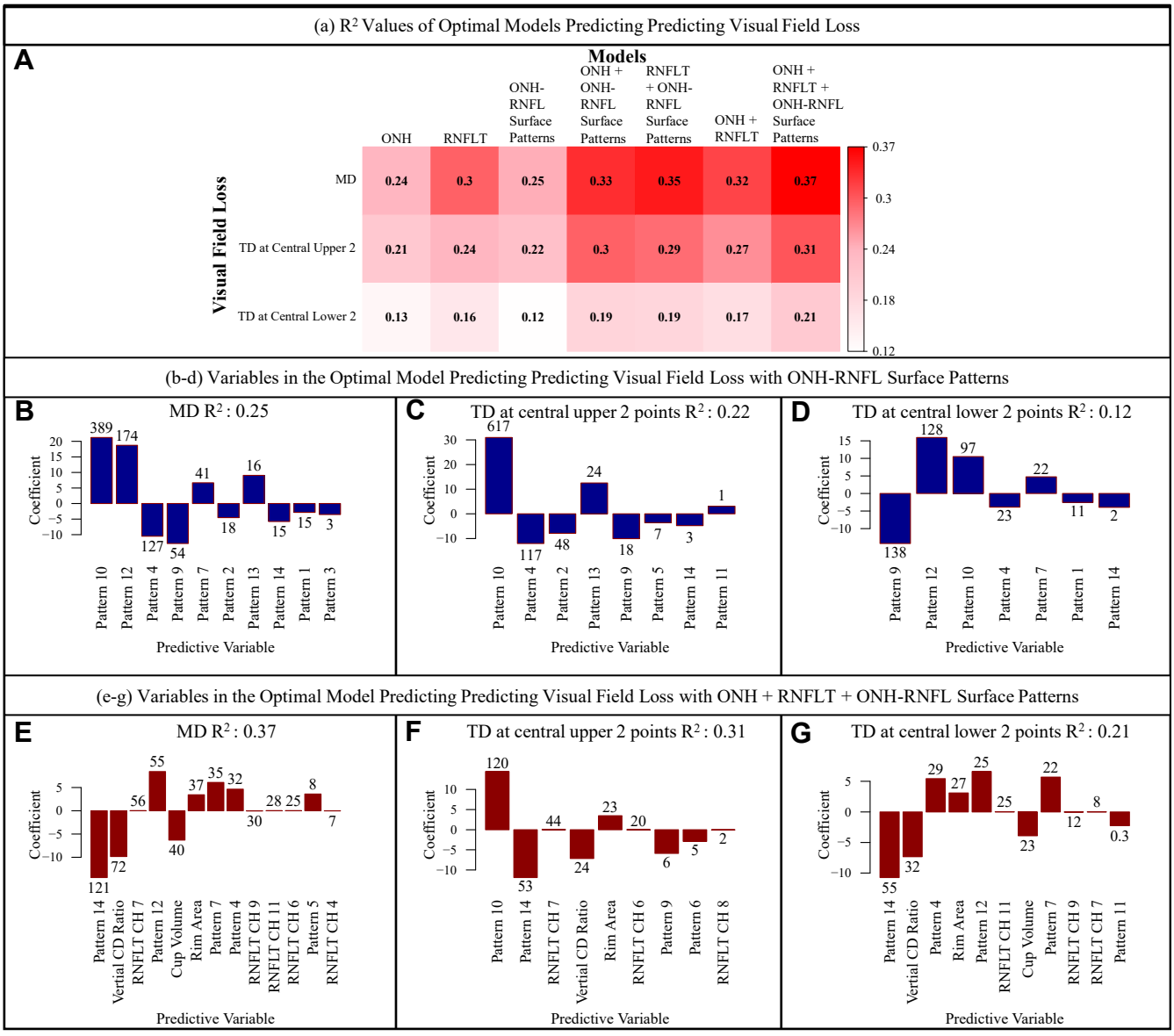

Figure 4. **A**, Heatmap showing adjusted r^2 values for different linear models that predicted the accompanied visual field (VF) loss using the 3 groups of structural features, including optic nerve head (ONH) summary parameters, clock-hour retinal nerve fiber layer thicknesses (RNFLTs), and ONH and retinal nerve fiber layer (RNFL) surface shape patterns, separately or in combination. **B**–**D**, Bar graphs showing the variables in the optimal model including only ONH and RNFL surface shape patterns that best predict the VF loss parameters. **E**–**G**, Bar graphs showing the variables in the optimal model when combining 3 groups of structural features, including ONH summary parameters, clock-hour RNFLTs, and ONH and RNFL surface shape patterns, that best predicted the VF loss. The numbers noted on top of the bars represent the respective statistical significance of each parameter, which were measured by the magnitude of Bayesian information criterion increase when that parameter was removed from the optimal model, and the direction of the bar represents the direction of the coefficient for that parameter when included in the optimal model. CD = cup-to-disc; CH = clock hour; MD = mean deviation; TD = total deviation.

pattern 12 (the superior para-ONH nerve thinning), higher pattern 4 (higher ILM in temporal inner regions around the ONH), and higher pattern 9 (higher ILM in inferior-nasal inner region around the ONH) coefficients; (2) for worse superior paracentral loss (Fig 4C), lower pattern 10 (the inferior para-ONH nerve thinning), higher pattern 4 (higher ILM in temporal inner regions around the ONH), higher pattern 2 (higher ILM in inferior-nasal peripheral regions around the ONH), and lower pattern 13 (lower ILM in superior peripheral region around the ONH) coefficients; and (3) for worse inferior paracentral loss (Fig 4D), higher pattern 9 (higher ILM in inferior-nasal inner region around the ONH), lower pattern 12 (the superior para-ONH nerve thinning), lower pattern 10 (the inferior para-ONH nerve thinning), and higher pattern 4 (higher ILM in temporal inner region around the ONH) coefficients. Although lower coefficients of pattern 10 (the inferior para-ONH nerve thinning) were associated with both superior and inferior

paracentral loss, lower coefficients of pattern 12 (the superior para-ONH nerve thinning) were associated only with inferior paracentral loss. Interestingly, higher coefficients of pattern 4 (higher ILM in the temporal inner region around the ONH) were associated with both superior and inferior paracentral loss. When combining the ONH and RNFL surface shape patterns with ONH summary parameters and 12 clock-hour RNFLTs, the top 5 most important parameters ($P < 0.001$ for all) for predicting various aspects of VF loss were (1) for worse MD (Fig 4E), higher coefficient of pattern 14 (shallow cups), higher vertical CDR, RNFL thinning of clock hour 7, lower pattern 12 coefficient (the superior para-ONH nerve thinning), and higher cup volume; (2) for worse superior paracentral loss (Fig 4F), lower pattern 10 coefficient (the inferior para-ONH nerve thinning), higher pattern 14 coefficient (shallow cups), RNFL thinning of clock hour 7, increased vertical CDR, and lower rim area; and (3) for worse inferior paracentral loss (Fig 4G), higher pattern 14 coefficient (shallow cups), increased vertical CDR, lower pattern 4 (higher ILM in the temporal inner region around the ONH region) coefficient, lower rim area, and lower pattern 12 coefficient (the superior para-ONH nerve thinning). Higher coefficients of patterns 10 (the inferior para-ONH nerve thinning) and 12 (the superior para-ONH nerve thinning) remained predictive of superior and inferior paracentral loss, respectively. It is interesting that worse VF loss was associated with higher pattern 14 (shallow cups), which became statistically more important in predicting VF loss when including ONH summary parameters and 12 clock-hour RNFLTs (BIC increases measuring parameters' statistical importance, changed from 15, 3, and 2 to 121, 53, and 55 for predicting the MD, TD at the central upper 2 locations, and TD at the central lower 2 locations, respectively).

Figure 5 shows the adjusted r^2 values of the optimal models to predict TD values at each of the 52 VF locations, using (1) ONH summary parameters, (2) clock-hour RNFLT, (3) the ONH and RNFL surface shape patterns, (4) ONH summary parameters and ONH and RNFL surface shape patterns, (5) clock-hour RNFLT and ONH and RNFL surface shape patterns, (6) ONH summary parameters and clock-hour RNFLT, and (7) ONH summary parameters, clock-hour RNFLTs, and ONH and RNFL surface shape patterns. The best model for predicting TD values was the model using the ONH parameters, RNFLT, and ONH and RNFL surface shape patterns with adjusted r^2 values ranging from 0.15 to 0.38. For all models, the variability in the superior-nasal VF region was predicted better than other VF regions. Figure 5H shows the improvement in adjusted r^2 value by the optimal models additionally using ONH and RNFL surface shape patterns compared with the optimal models using ONH summary parameters and clock-hour RNFLT. The improvement in adjusted r^2 values ranged from 0.02 to 0.05. The improvement was more substantial in the inferior and inferonasal VF regions and was less substantial in the superior and superotemporal VF regions based on the BIC decrease (greater BIC decrease indicates stronger evidence that additionally using ONH and RNFL surface shape patterns improved VF prediction) at each location shown in Figure 5I.

The ONH and RNFL Surface Shape Patterns and Prediction of Subsequent VF Loss Rates

Eighty eyes from 64 participants with an average follow-up of 4.1 ± 2.0 years with at least 5 VF measurements were used for our longitudinal analyses. Mean age and MD at baseline were 62.5 ± 14.2 years and −5.8 ± 5.7 dB, respectively. Figure 6A shows the heatmap of adjusted r^2 values for linear models that predicted various metrics of VF loss rate using the 3 groups of structural features, including ONH summary parameters, clock-hour RNFLT, and ONH and RNFL surface shape patterns separately or in combination. The VF loss rate metrics included MD slope and pointwise TD slope at the 2 superior paracentral locations and the 2 inferior paracentral locations. Using ONH and RNFL surface shape patterns in addition to ONH summary parameters and 12 clock-hour RNFLTs led to an improvement in the prediction of MD slope (r^2 from 0 to 0.13; BIC decrease, 8) and superior (r^2 from 0.13 to 0.15; BIC decrease, 1) and inferior (r^2 from 0 to 0.16; BIC decrease, 8) paracentral loss longitudinally. The prediction improvement for predicting overall MD slope and TD slope at the central lower 2 locations based on the model comparison using BIC was significant, whereas the improvement for predicting TD slope at the central upper 2 locations was indistinguishable.

When combining ONH summary parameters, 12 clock-hour RNFLTs, and ONH and RNFL surface shape patterns to predict VF loss rate parameters and removing redundant features by model selection with BIC, only ONH and RNFL surface shape patterns remained predictive ($P < 0.05$ for all) of VF loss rate parameters (Fig 6B–D). Specifically, MD worsening was associated with higher coefficients of pattern 9 (higher ILM in the inferior-nasal inner region around the ONH region) and lower coefficients of pattern 6 (lower ILM in the temporal peripheral region around the ONH region); TD worsening at the central upper 2 locations was associated with higher coefficients of pattern 9 (higher ILM in the inferior-nasal inner region around the ONH region) and lower coefficients of pattern 6 (lower ILM in the temporal peripheral region around the ONH region) and pattern 1 (lower ILM in the superior peripheral region around the ONH region); TD worsening at the central lower 2 locations was correlated with higher coefficients of pattern 9 (higher ILM in the inferior-nasal inner region around the ONH region) and lower coefficients of pattern 6 (lower ILM in the temporal peripheral region around the ONH region). For the linear modeling results for the subsequent VF loss rates based on the less stringent model selection using the Akaike information criterion, see Supplemental Figures 2 and 3.

Discussion

We identified 14 patterns from the ONH and RNFL surface shape structure represented by the ILM boundary and its continuation in the ONH region based on the segmentation provided by the device, with NMF, an unsupervised AI method. Each ONH and RNFL surface shape structure can be decomposed into a linear combination of the 14 patterns,

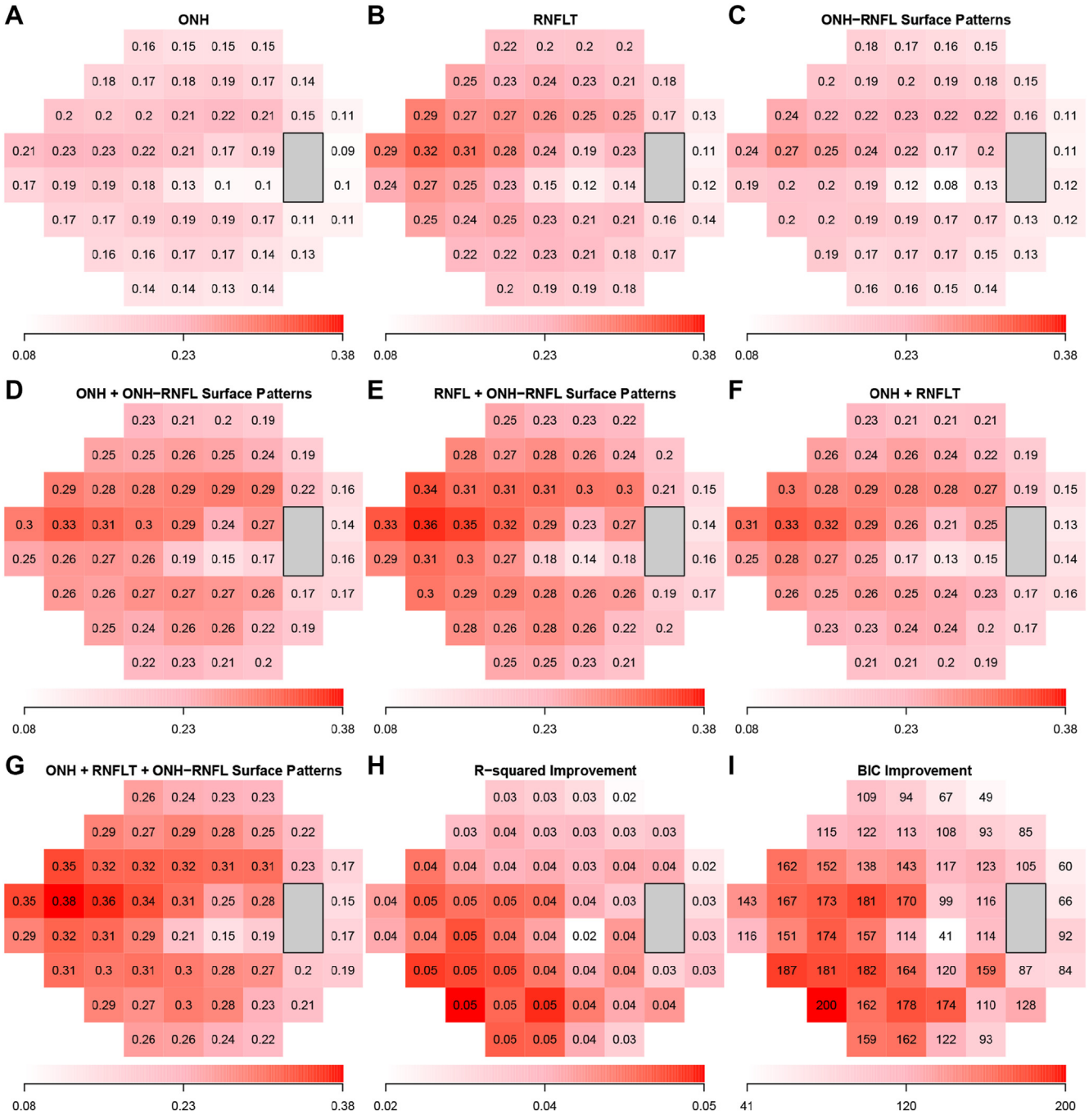

Figure 5. **A**–**G**, Adjusted r^2 values of the optimal models to predict total deviation (TD) values at each of the 52 visual field locations, using (**A**) optic nerve head (ONH) summary parameters, (**B**) clock-hour retinal nerve fiber layer thicknesses (RNFLTs), (**C**) the ONH and retinal nerve fiber layer (RNFL) surface shape patterns, (**D**) ONH summary parameters and ONH and RNFL surface shape patterns, (**E**) clock-hour RNFLTs and ONH and RNFL surface shape patterns, (**F**) ONH summary parameters and clock-hour RNFLTs, and (**G**) ONH summary parameters, clock-hour RNFLTs, and ONH and RNFL surface shape patterns. The best model for predicting TD values was the model using the ONH parameters, RNFLT, and ONH and RNFL surface shape patterns with adjusted r^2 values ranging from 0.15 to 0.38. **H and I**, Improvement in adjusted r^2 value and BIC statistic decrease by using the optimal models additionally using ONH and RNFL surface shape patterns, compared with the optimal models using ONH summary parameters and clock-hour RNFLTs only. BIC = Bayesian information criterion.

and a higher coefficient for an ONH and RNFL surface shape pattern type indicated higher ILM position in the relatively informative regions (red and yellow regions) for that ONH and RNFL surface shape pattern and vice versa.

Glaucoma causes irreversible loss of retinal ganglion cells and their axons affecting the ILM position, and this leads to alteration in the anatomic features of the ONH region.[23–25] Furthermore, the associated axonal degeneration is related

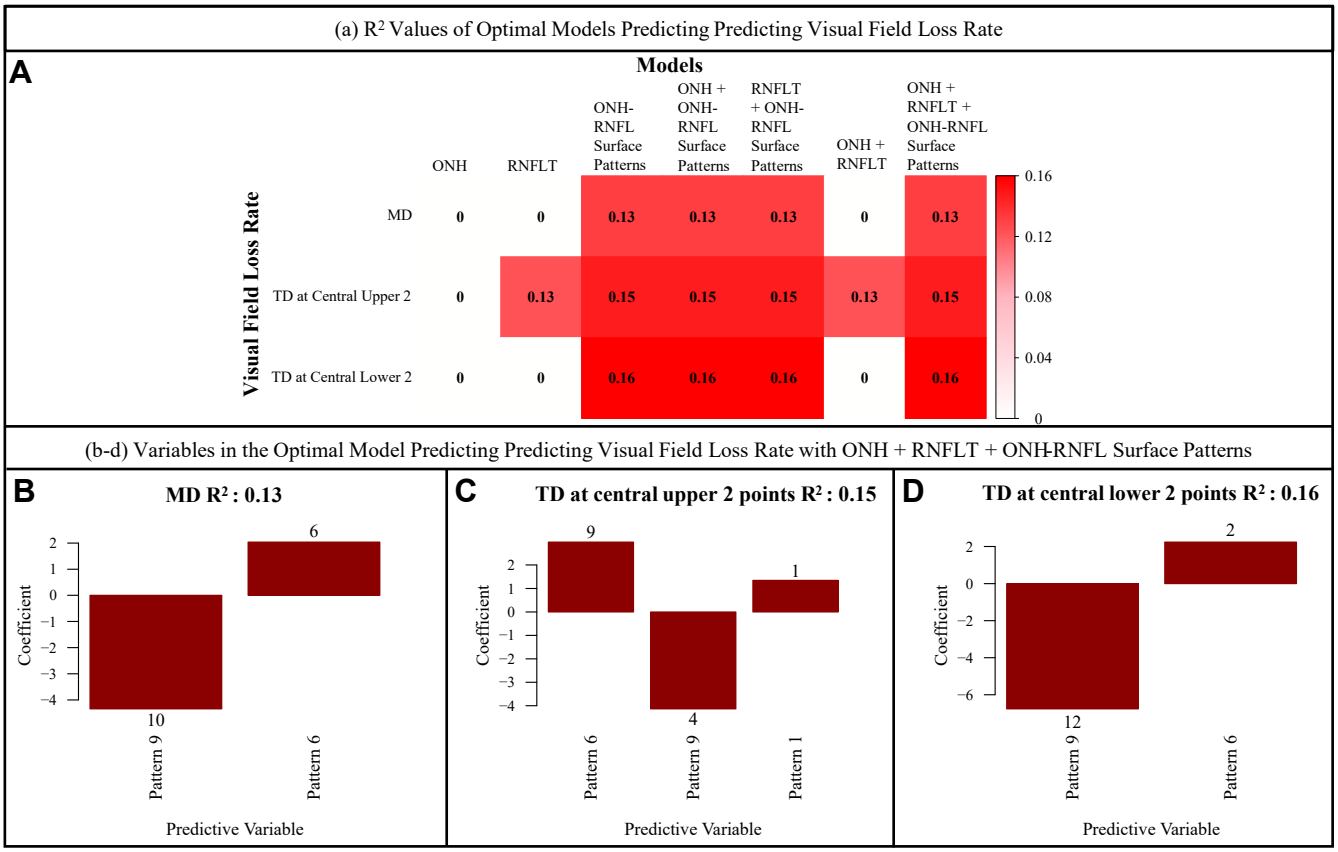

Figure 6. **A**, Heatmap showing adjusted r^2 values for linear models that predicted various metrics of visual field loss rate using the 3 groups of structural features, including optic nerve head (ONH) summary parameters, clock-hour retinal nerve fiber layer thicknesses (RNFLTs), and ONH and retinal nerve fiber layer (RNFL) surface shape patterns separately or in combination. **B**–**D**, Variables in the optimal model combining 3 groups of structural features, including ONH summary parameters, clock-hour RNFLTs, and ONH and RNFL surface shape patterns, that best predicted (**B**) the visual field mean deviation (MD) loss rate, (**C**) the total deviation (TD) loss rate at the upper 2 central points, and (**D**) the TD loss rate at the lower 2 central points.

closely to morphologic changes in the surrounding connective tissue structures, such as the lamina cribrosa.[26,27] Traditionally, the ONH structural features, including CDR, disc tilt, disc ovality, and disc torsion, are assessed based on 2-D fundus imaging.[1,28–31] With the advent of SD OCT devices, we now can visualize and quantify 3-D ONH structures, including Bruch's membrane opening, lamina cribrosa, scleral thickness, and 3-D neuroretinal rim parameters.[3,5,8,32] Three-dimensional neuroretinal rim parameters like the minimum distance band, Bruch's membrane opening–minimum rim width, and 3-D rim volume have outperformed conventional neuroretinal parameters like RNFLT to diagnose glaucoma.[32,33] The Cirrus SD OCT device provides robust automatic segmentation of the ILM boundary representing 3-D ONH and RNFL surface shape structure.[34] More importantly, the variation of the ONH and RNFL surface shape structure encodes both the axonal loss and the remodeling of the lamina cribrosa. The ONH and RNFL surface shape can be affected by both RNFL thinning and the recess of the lowest ILM position possibly because of the thinning of the prelaminar tissue and deformation of the lamina cribrosa.

Interest is growing in using information from the OCT scans and training deep learning models to apply the information obtained in glaucoma care.[35–37] For instance, Christopher et al[37] used deep learning models trained on RNFLT maps obtained from SD OCT to differentiate eyes with and without glaucomatous VF damage and showed that their deep learning model had high accuracy in identifying eyes with glaucomatous VF damage and predicting the severity of functional loss; however, most previous work has relied on RNFLT rather than the 3-D ONH structure. In 2021, Panda et al[11] described a deep learning approach using autoencoders to identify 3-D structural biomarkers in ONH anatomic features; however, unlike our work, their analyses required manual delineation of the 3-D OHN structure. Furthermore, the relationship between structural phenotypes determined from the reduced features generated by the customized autoencoder and the 3-D ONH structures are complex to understand fully. In contrast, our ONH and RNFL surface shape patterns determined by NMF are more clinically interpretable because NMF is specialized in learning patterns with sparse and regional features from nonnegative data.

We correlated ONH and RNFL surface shape patterns with various established glaucoma diagnostic parameters and OCT parameters, including VF MD, glaucoma diagnosis, IOP, spherical equivalent refractive error, and ONH summary parameters from the OCT analysis report. Specifically, we showed that thinner inferior and clock hour 7

RNFLT were associated most with lower coefficients of pattern 10 ($r = 0.42$ and $r = 0.35$, respectively) representing the inferior para-ONH nerve thinning. Inferior RNFLT and clock hour 7 RNFLT demonstrated high specificity and sensitivity to detect glaucomatous VF defects. The clock hour 7 sector is adjacent to the inferior vulnerability zone proposed by Budenz et al[38] and Hood.[39] Similarly, we observed that thinner average global RNFLT and thinner RNFLT in clock hours 11 and 12 were correlated with lower coefficients of patterns 12 ($r = 0.21$, $r = 0.22$, and $r = 0.2$, respectively), representing the superior para-ONH nerve thinning. Retinal nerve fiber layer thicknesses in clock hours 11 and 12 have high area under the receiver operating characteristic curve for identifying glaucomatous VF loss and are in proximity to the superior vulnerability zone proposed by Budenz et al[38] and Hood.[39] Worse VF MD and thinner average global RNFLT were correlated most with lower coefficients of patterns 10 and 12 ($r = 0.29$ and $r = 0.28$, respectively), representing RNFL loss in the inferior and superior para-ONH regions, which is in agreement with the clinical relevance of vertical CDR in diagnosing glaucoma.[40]

A particularly important finding is that VF MD (Fig 3) was associated inversely ($P < 0.001$ for all) with patterns 5 ($r = -0.16$), 4 ($r = -0.13$), 9 ($r = -0.13$), 2 ($r = -0.12$), and 6 ($r = -0.12$), and thus, a worse MD was associated with higher coefficients of these patterns, representing higher ILM in the red and yellow regions of the respective patterns. Because structural thinning of the RNFL in glaucoma is known to lower ILM vertical positions, the correlations between higher regional ILM position and worse MD imply that the cup shape patterns with higher regional ILM position may be another marker of VF damage in glaucoma. In our multivariate linear regression analyses using the 14 ONH and RNFL surface shape patterns, worse VF MD was associated with higher pattern 4 (higher ILM in the temporal inner regions around the ONH) and higher pattern 9 (higher ILM in the inferior-nasal inner region around the ONH) coefficients. Furthermore, worse superior paracentral loss was associated with higher pattern 4 (higher ILM in the temporal inner regions around the ONH) and higher pattern 2 (higher ILM in the inferior-nasal peripheral regions around the ONH) coefficients, and worse inferior paracentral loss was associated with higher pattern 9 (higher ILM in the inferior-nasal inner region around the ONH) coefficients. This suggests that a higher ILM in these areas is associated with VF loss, which is contrary to what is understood clinically; that is, RNFL thinning should result in lower ILM vertical position. A concern exists that the reference point of the lowest ILM position can be recessed because of glaucomatous structural changes, including the prelaminar tissue thinning and lamina cribrosa deformation, which results in higher ILM positions outside the optic cup that are related to worse VF loss we observed in this study; however, if that is the case, we would not have been able to observe that higher ILM positions represented by higher coefficients of patterns 4, 9, and 2 (Fig 4B) were associated with worse MD in the multivariate regression using all 14 ONH and RNFL surface shape patterns, among which the variation of the coefficients for patterns 10, 12, and 14 would be able to represent the recession of the lowest ILM position. Our results suggest that this type of ONH and RNFL surface shape pattern with higher regional ILM position may be an anatomic risk factor for VF damage in glaucoma, which would need to be validated further in a larger longitudinal study.

Myopia has been associated with glaucoma, and prior studies have shown that patients with myopia have a two- to sevenfold increased risk of glaucoma compared with those without myopia.[41,42] In our study, we found that a more negative spherical equivalent representing myopia was correlated most with lower coefficients of pattern 6 ($r = 0.11$), representing lower ILM in the temporal peripheral region, and with higher coefficients of pattern 1 ($r = -0.13$), representing higher ILM in the superior peripheral region, which may be explained by disc tilt, and thus highlighting that ONH and RNFL surface shape patterns could encode variance in anatomic structures related to myopia. This is consistent with previous studies in which authors have identified that tilted optic discs are associated with higher myopia.[43]

The addition of ONH and RNFL surface shape patterns to ONH summary parameter and 12 clock-hour RNFLTs improved the prediction of accompanied VF MD slope (r^2 from 0.32 to 0.37) and superior (r^2 from 0.27 to 0.31) and inferior (r^2 from 0.17 to 0.21) paracentral loss. We showed that lower coefficients of patterns 10 and 12 (the inferior and superior para-ONH nerve thinning) were related most to the global VF loss of MD (Fig 4B). Only inferior para-ONH nerve thinning (lower pattern 10) is relevant to superior paracentral loss (Fig 4C), whereas both inferior and superior para-ONH nerve thinning (lower patterns 10 and 12) were relevant to inferior paracentral loss (Fig 4D). Consistent with our correlation analyses in Figure 3, we observed that higher ILM positions (Figs 4B–D) were relevant to worse MD (patterns 4 and 9, higher ILM in temporal inner regions and inferior-nasal inner region around the ONH), superior paracentral loss (patterns 4 and 2, higher ILM in temporal inner regions and inferior-nasal peripheral regions around the ONH), and inferior paracentral loss (pattern 9, higher ILM in inferior-nasal inner region around the ONH). In a smaller subgroup with at least 5 VF measurements available longitudinally, we showed that using ONH and RNFL surface shape patterns in addition to ONH summary parameter and 12 clock-hour RNFLTs led to improvement in the prediction of overall VF loss and inferior paracentral VF loss over time, assessed by both BIC and Akaike information criterion scores. In general, worse VF loss rate (global, superior, and inferior paracentral) was associated with higher coefficients of pattern 9 (higher ILM in inferior-nasal inner region around the ONH) and lower coefficients of pattern 6 (lower ILM in the temporal peripheral region around the ONH). None of the established ONH summary parameters and clock-hour RNFLTs remained in the optimal model predicting the VF loss rate. Our results suggest that the ONH and RNFL surface shape patterns may be a more useful risk factor for predicting glaucoma progression.

Our study has the following limitations. First, our analysis was based solely on OCT scans obtained from the Cirrus SD

OCT device. In the future, we also would like to validate our results using OCT scans from other devices such as Spectralis and Topcon. Second, the ILM could have overlapped vertically in rare cases. Our model did not address this issue because of the limitation of the heatmap-type analyses. For some scans, a slight tilt in the head positioning of the study participant while obtaining the scan may have affected the measurements and the tilt observed in the ONH and RNFL surface shape patterns. Additionally, we did not acquire information on the lens status of the patients at the time of imaging, and it is possible that some patients may have been pseudophakic, and thus, spherical equivalent values may not be valid in these cases. Additionally, our sample size for prediction of VF loss rate was relatively small, and more data with longitudinal measurements will be needed to validate fully the usefulness of ONH and RNFL surface shape patterns for predicting future VF loss rates. Finally, although our results state that eyes with higher ILM in certain regions could be more vulnerable to glaucomatous VF loss, we need to validate this speculation more rigorously. It will be helpful to conduct a population-based study to observe the natural history of glaucoma development to see if higher ILM positions in certain regions are indeed related to subsequent glaucoma development and VF loss.

In conclusion, we showed that ONH and RNFL surface shape patterns determined by unsupervised AI techniques were associated significantly with established glaucoma diagnostics and structural and functional parameters. Inclusion of ONH and RNFL surface shape patterns improved the structure−function relationship and prediction of subsequent VF loss rate in addition to ONH summary parameters and RNFLT measurements.

Footnotes and Disclosures

Originally received: January 21, 2022.
Final revision: March 30, 2022.
Accepted: April 12, 2022.
Available online: April 20, 2022. Manuscript no. XOPS-D-22-00010

[1] Department of Ophthalmology, Massachusetts Eye and Ear, Harvard Medical School, Boston, Massachusetts.

[2] Eye and Vision Research Institute, Icahn School of Medicine at Mount Sinai, New York, New York.

[3] Harvard Ophthalmology AI Lab, Schepens Eye Research Institute of Massachusetts Eye and Ear, Harvard Medical School, Boston, Massachusetts.

[4] State Key Laboratory of Ophthalmology, Zhongshan Ophthalmic Center, Sun Yat-Sen University, Guangzhou, Guangdong, China.

Disclosure(s):

All authors have completed and submitted the ICMJE disclosures form.

The author(s) have made the following disclosure(s): L.R.P.: Consultant − Twenty-Twenty Therapeutics, Eyenovia, Skye Biosciences

M.V.B.: Consultant − Carl Zeiss Meditec, Topcon; Lecturer − Carl Zeiss Meditec

Supported by the Glaucoma Foundation, New York, New York (unrestricted challenge grant [L.R.P.]); the National Institutes of Health, Bethesda, Maryland (grant nos.: R01 EY030575 [T.E.], K99 EY028631 [M.W.], R00 EY028631 [M.W.], and P30 EY003790 [M.F., Y.L., M.E., T.E., M.W.]); Research to Prevent Blindness, Inc., New York, New York (departmental grant) [M.W.]; an Alcon Young Investigator Grant [M.W.]; and Genentech, Inc., South San Francisco, California [M.W.].

HUMAN SUBJECTS: Human subjects were included in this study. Massachusetts Eye and Ear institutional review board approved the study. All research adhered to the tenets of the Declaration of Helsinki. Given the retrospective nature of the study, the need for informed consent was waived.

No animal subjects were included in this study.

Author Contributions:

Conception and design: Saini, Wang

Analysis and interpretation: Saini, Shen, Pasquale, Boland, Friedman, Zebardast, Fazli, Li, Eslami, Elze, Wang

Data collection: Saini, Wang

Obtained funding: N/A; Study was performed as part of the authors' regular employment duties. No additional funding was provided.

Overall responsibility: Saini, Shen, Pasquale, Boland, Friedman, Zebardast, Fazli, Li, Eslami, Elze, Wang

Abbreviations and Acronyms:
AI = artificial intelligence; **BIC** = Bayesian information criterion; **CDR** = cup-to-disc ratio; **dB** = decibels; **ILM** = inner limiting membrane; **IOP** = intraocular pressure; **MD** = mean deviation; **NMF** = nonnegative matrix factorization; **ONH** = optic nerve head; **RNFL** = retinal nerve fiber layer; **RNFLT** = retinal nerve fiber layer thickness; **SD** = spectral-domain; **TD** = total deviation; **3-D** = 3-dimensional; **2-D** = 2-dimensional; **VF** = visual field.

Keywords:
Glaucoma, OCT, Structure−function relationship, Unsupervised artificial intelligence, Visual field loss rate prediction.

Correspondence:
Mengyu Wang, PhD, Massachusetts Eye and Ear, 20 Staniford Street, Boston, MA 02114. E-mail: mengyu_wang@meei.harvard.edu.

References

1. Tuulonen A, Airaksinen PJ. Initial glaucomatous optic disk and retinal nerve fiber layer abnormalities and their progression. *Am J Ophthalmol*. 1991;111(4):485−490.
2. Leung CKS, Lam S, Weinreb RN, et al. Retinal nerve fiber layer imaging with spectral-domain optical coherence tomography: analysis of the retinal nerve fiber layer map for glaucoma detection. *Ophthalmology*. 2010;117(9):1684−1691.
3. Reis ASC, Sharpe GP, Yang H, et al. Optic disc margin anatomy in patients with glaucoma and normal controls with spectral domain optical coherence tomography. *Ophthalmology*. 2012;119(4):738−747.
4. Sanchez-Galeana C, Bowd C, Blumenthal EZ, et al. Using optical imaging summary data to detect glaucoma. *Ophthalmology*. 2001;108(10):1812−1818.
5. Inoue R, Hangai M, Kotera Y, et al. Three-dimensional high-speed optical coherence tomography imaging of lamina cribrosa in glaucoma. *Ophthalmology*. 2009;116(2):214−222.

6. Omodaka K, Horii T, Takahashi S, et al. 3D evaluation of the lamina cribrosa with swept-source optical coherence tomography in normal tension glaucoma. *PLoS ONE*. 2015;10(4):1−16.
7. Takayama K, Hangai M, Kimura Y, et al. Three-dimensional imaging of lamina cribrosa defects in glaucoma using swept-source optical coherence tomography. *Invest Ophthalmol Vis Sci*. 2013;54(7):4798−4807.
8. Lopilly Park HY, Lee NY, et al. Measurement of scleral thickness using swept-source optical coherence tomography in patients with open-angle glaucoma and myopia. *Am J Ophthalmol*. 2014;157(4):876−884.
9. Park HYL, Shin HY, Park CK. Imaging the posterior segment of the eye using swept-source optical coherence tomography in myopic glaucoma eyes: comparison with enhanced-depth imaging. *Am J Ophthalmol*. 2014;157(3):550−557.
10. Wang YX, Yang H, Luo H, et al. Peripapillary scleral bowing increases with age and is inversely associated with peripapillary choroidal thickness in healthy eyes. *Am J Ophthalmol*. 2020;217:91−103.
11. Panda SK, Cheong H, Tun TA, et al. Describing the structural phenotype of the glaucomatous optic nerve head using artificial intelligence. *Am J Ophthalmol*. 2022;236:172−182.
12. Lee DD, Seung HS. Learning the parts of objects by non-negative matrix factorization. *Nature*. 1999;401(6755):788−791.
13. Lee DD, Seung HS. Algorithms for non-negative matrix factorization. In: Leen TK, Dietterich TG, Tresp V, eds. MIT Press, Massachusetts. *Advances in Neural Information Processing Systems*. 2001;13:556−562.
14. Hardin JS, Taibbi G, Nelson SC, et al. Factors affecting Cirrus-HD OCT optic disc scan quality: a review with case examples. In: Ryan SJ, ed. London and New York: Saunders/Elsevier. *J Ophthalmol*. 2015:746150.
15. Carl Zeiss Meditec. *Inc. Cirrus HD-OCT User Manual—Models*. Dublin, CA: Carl Zeiss Meditec, Inc.; 2015, 500, 5000.
16. Sebag J, Green RW. Vitreous and vitreoretinal interface. *Retina Fifth Edition*. 2013;1:482−516.
17. Heegaard S, Jensen OA, Prause JU. Structure and composition of the inner limiting membrane of the retina—SEM on frozen resin-cracked and enzyme-digested retinas of Macacca mulatta. *Graefes Arch Clin Exp Ophthalmol*. 1986;224(4):355−360.
18. Birt CM, Shin DH, Samudrala V, et al. Analysis of reliability indices from Humphrey visual field tests in an urban glaucoma population. *Ophthalmology*. 1997;104(7):1126−1130.
19. Newkirk MR, Gardiner SK, Demirel S, Johnson CA. Assessment of false positives with the Humphrey Field Analyzer II perimeter with the SITA algorithm. *Invest Ophthalmol Vis Sci*. 2006;47(10):4632−4637.
20. Elze T, Pasquale LR, Shen LQ, et al. Patterns of functional vision loss in glaucoma determined with archetypal analysis. *J R Soc Interface*. 2015;12(103):20141118.
21. Wang M, Shen LQ, Pasquale LR, et al. An artificial intelligence approach to assess spatial patterns of retinal nerve fiber layer thickness maps in glaucoma. *Transl Vis Sci Technol*. 2020;9(9):1−12.
22. Glickman ME, Rao SR, Schultz MR. False discovery rate control is a recommended alternative to Bonferroni-type adjustments in health studies. *J Clin Epidemiol*. 2014;67(8):850−857.
23. Quigley HA, Green WR. The histology of human glaucoma cupping and optic nerve damage: clinicopathologic correlation in 21 eyes. *Ophthalmology*. 1979;86(10):1803−1827.
24. Quigley HA, Addicks E, Green RW. Optic nerve damage in human glaucoma in glaucoma, ischemic neuropathy, papilledema, and toxic neuropathy. *Arch Ophthalmol*. 1982;100:135−146.
25. Varma R, Quigley HA, Ellen Pease M. Changes in optic disk characteristics and the number of nerve fibers in experimental glaucoma. *Am J Ophthalmol*. 1992;114(5):554−559.
26. Ren R, Wang N, Li B, et al. Lamina cribrosa and peripapillary sclera histomorphometry in normal and advanced glaucomatous chinese eyes with various axial length. *Invest Ophthalmol Vis Sci*. 2009;50(5):2175−2184.
27. Quigley HA, Addicks EM. Regional differences in the structure of the lamina cribrosa and their relation to glaucomatous optic nerve damage. *Arch Ophthalmol*. 1981;99(1):137−143.
28. Park HYL, Lee K, Park CK. Optic disc torsion direction predicts the location of glaucomatous damage in normal-tension glaucoma patients with myopia. *Ophthalmology*. 2012;119(9):1844−1851.
29. Park HYL. Choi S il, Choi JA, Park CK. Disc torsion and vertical disc tilt are related to subfoveal scleral thickness in open-angle glaucoma patients with myopia. *Invest Ophthalmol Vis Sci*. 2015;56(8):4927−4935.
30. Lee JE, Sung KR, Lee JY, Park JM. Implications of optic disc tilt in the progression of primary open-angle glaucoma. *Invest Ophthalmol Vis Sci*. 2015;56(11):6925−6931.
31. Kwun Y, Han G, Choy YJ, et al. Optic disc characteristics and visual field progression in normal tension glaucoma patients with tilted optic discs. *J Glaucoma*. 2016;25(11):901−907.
32. Fan KC, Tsikata E, Khoueir Z, et al. Enhanced diagnostic capability for glaucoma of 3-dimensional versus 2-dimensional neuroretinal rim parameters using spectral domain optical coherence tomography. *J Glaucoma*. 2017;26(5):450−458.
33. Shieh E, Lee R, Que C, et al. Diagnostic performance of a novel three-dimensional neuroretinal rim parameter for glaucoma using high-density volume scans. *Am J Ophthalmol*. 2016;169:168−178.
34. Mylonas G, Ahlers C, Malamos P, et al. Comparison of retinal thickness measurements and segmentation performance of four different spectral and time domain OCT devices in neovascular age-related macular degeneration. *Br J Ophthalmol*. 2009;93(11):1453−1460.
35. Larrosa JM, Polo V, Ferreras A, et al. Neural network analysis of different segmentation strategies of nerve fiber layer assessment for glaucoma diagnosis. *J Glaucoma*. 2015;24(9):672−678.
36. Muhammad H, Fuchs TJ, de Cuir N, et al. Hybrid deep learning on single wide-field optical coherence tomography scans accurately classifies glaucoma suspects. *J Glaucoma*. 2017;26(12):1086−1094.
37. Christopher M, Bowd C, Belghith A, et al. Deep learning approaches predict glaucomatous visual field damage from OCT optic nerve head en face images and retinal nerve fiber layer thickness maps. *Ophthalmology*. 2020;127(3):346−356.
38. Budenz DL, Michael A, Chang RT, et al. Sensitivity and specificity of the StratusOCT for perimetric glaucoma. *Ophthalmology*. 2005;112(1):3−9.
39. Hood DC. Improving our understanding, and detection, of glaucomatous damage: an approach based upon optical

coherence tomography (OCT). *Prog Retin Eye Res*. 2017;57(1):46–75.
40. Kirsch RE, Anderson DR. Clinical recognition of glaucomatous cupping. *Am J Ophthalmol*. 1973;75(3):442–454.
41. Mitchell P, Hourihan F, Sandbach J, Jin Wang J. The relationship between glaucoma and myopia. *Ophthalmology*. 1999;106(10):2010–2015.
42. Xu L, Wang Y, Wang S, et al. High myopia and glaucoma susceptibility. The Beijing Eye Study. *Ophthalmology*. 2007;114(2):216–220.
43. Hwang YH, Yoo C, Kim YY. Myopic optic disc tilt and the characteristics of peripapillary retinal nerve fiber layer thickness measured by spectral-domain optical coherence tomography. *J Glaucoma*. 2012;21(4):260–265.